MDPI

Article

Non-Isolated DC-DC Converters in Fuel Cell Applications: Thermal Analysis and Reliability Comparison

Omid Alavi [1,2,3,*] **, Talieh Rajabloo** [1,2,3] **, Ward De Ceuninck** [1,2,3] **and Michaël Daenen** [1,2,3]

1   IMO-IMOMEC, Hasselt University, Wetenschapspark 1, 3590 Diepenbeek, Belgium;
    talieh.rajabloo@uhasselt.be (T.R.); ward.deceuninck@uhasselt.be (W.D.C.);
    michael.daenen@uhasselt.be (M.D.)
2   Imec, Kapeldreef 75, 3001 Heverlee, Belgium
3   EnergyVille, Thor Park 8310, 3600 Genk, Belgium
*   Correspondence: omid.alavi@uhasselt.be; Tel.: +32-11-26-88-26

Abstract: An alternative energy source that has appeared beyond expectations and has seen a lot of progress is the fuel cell. A proton exchange membrane (PEM) fuel cell is chosen for analysis and requires a DC-DC boost converter as an interface between the fuel cell and the load to provide a high-gain regulated voltage. Although great effort towards developing different converter topologies has been made during recent decades, less attention has been devoted to the reliability and thermal performance assessment of the present converters. In this paper, five non-isolated DC-DC converters are analyzed in terms of both thermal behavior and reliability. The temperature estimation of semiconductor devices as a critical part of the thermal analysis has been made via a detailed thermal model and the reliability is evaluated by means of a power cycling test. Finally, a performance score has been attributed using the TOPSIS ranking methodology and considering all the criteria (e.g., the number of components and cost) at the same time. The results indicated that the floating interleaved boost converter is always at the top of the list, even if the weight of the indicators is changed. When the weight of the cost criterion is higher than the reliability criterion, the multi-switch boost converter will be in second place. If the weight of the reliability criterion is greater than cost, the interleaved and multi-switch converter are ranked second and third, respectively. Additionally, the Cuk converter with a closeness coefficient of zero is always associated with the most unfavorable performance.

Keywords: fuel cell; DC-DC converter; Norris–Landzberg; power modules; proton exchange membrane; reliability; thermal analysis

1. Introduction

Population growth and the excessive use of electrical appliances have an enormous influence on electricity consumption mainly coming from fossil fuels. Alternative energy sources have gained considerable attention in many countries in recent decades, owing primarily to greenhouse gas emissions, global warming, and ozone layer depletion. Although there is a great effort to replace all the traditional energy sources with wind and solar energies, fuel cells are becoming even more important and have gained a favorable position as a leading source of power. Moreover, fuel cells are one of the effective technologies to integrate green hydrogen into the power system. Given the fact that the fuel cell is compact, lightweight, and non-polluting, it is very suitable for applications such as electric vehicles and emergency power systems [1].

Compared to wind and solar power generation, the advantage of using a fuel cell is that it can be used anywhere as there are no environmental or geographical constraints to use it [2]. These features have enabled fuel cells to be used from watts to megawatts for applications such as the space industry [3], portable applications [4], remote area power supplies [5], and communication applications [6].

Among the different types of fuel cells, proton exchange membrane fuel cells (PEM-FCs), with characteristics such as low operating temperature, high power density, low cost, and fast response, are the most attractive option for electric vehicles and residential applications [7]. A PEM fuel cell uses a solid polymer as an electrolyte which only needs hydrogen and oxygen from the air. After generating electrochemical energy, the only resulting by-product is water [8].

However, a power conditioning system for fuel cells still encounters several problems due to the small and non-regulated voltage produced at the output of the fuel cell. Therefore, the use of power electronic converters in order to step up/regulate the output voltage level to the desired voltage and reduce the current ripple is necessary [9]. Using these converters as an advantage, the number of cells used within the fuel cell can be reduced [10]. The behavior of the fuel cell is nonlinear, which is why its output voltage should be initially increased by a DC-DC boost converter to feed the load, or a grid-tie inverter can be connected to the boost converter through a DC-link. Although transformer-based DC-DC converters are commonly used to step up the voltage level, these converters will increase the weight and cost of the entire fuel cell system, which is not desirable [11]. Another important issue to consider is that a high-level current ripple can accelerate the aging of the electrodes since the efficiency of transportation is reduced in an aged electrode [12]. The input current for a buck-boost power converter is discontinuous or pulsating; thus, it is recommended to use step-up converters with an input inductor for a fuel cell to minimize the current ripple [13]. Nevertheless, it is important to choose a power electronic converter that has a longer lifetime and greater reliability while meeting the cost and performance requirements.

The primary purpose of this paper is to evaluate five different non-isolated (transformerless) DC-DC step-up converters—including the conventional boost, interleaved boost, floating-interleaved boost, multi-switch boost, and Cuk converter—in terms of both thermal and reliability aspects. In the first stage, a detailed thermal model will be used to estimate the accurate values of junction temperatures. Then, a power cycling test will be done by applying a periodic power with a frequency of 1 Hz to the power semiconductors, after which, the gathered temperature variations will be used to calculate the number of cycles to failure as perhaps the most significant factor concerning their reliability and lifetime. A ranking methodology will be adopted with the aim to bring into focus the important indicators (the number of cycles to failure, highest junction temperatures, the number of components, and cost) for selecting the most appropriate converter for use on fuel cell applications.

The rest of the paper is organized as follows. Section 2 gives a detailed description of the PEM fuel cell and its relationships. The equations related to the different DC-DC boost converter topologies are addressed in Section 3. The proposed thermal model for accurate estimation of power semiconductors' junction temperature is described in Section 4. Section 5 presents all the information related to the power cycling test procedure and reliability evaluation. The results and discussion are presented in Section 6, and finally, the conclusion is drawn in Section 7.

2. Fuel Cell

Among the various types of fuel cells, proton exchange membrane fuel cells (PEMFCs) have attracted much attention in recent years since they can operate at relatively low temperatures with a fast start-up [14]. The process of generating electricity from a PEM fuel cell is linked to chemical reactions that lead to electron transfer. These chemical reactions can be divided into two categories: oxidation (emission of electrons) and reduction (absorption of electrons). In the PEM fuel cells, an acidic polymer membrane is used as the electrolyte and the chemical reactions that produce electricity take place at the electrodes based on the following reactions [15]:

$$\text{Oxidation: } H_2 \rightarrow 2H^+ + 2e^-$$

$$\text{Reduction: } 4H^+ + O_2 + 4e^- \rightarrow 2H_2O$$
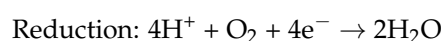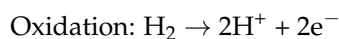
To achieve the overall reaction, the first equation (oxidation reaction) must be doubled and then summed up with the second one (reduction reaction), as the number of electrons is the same on both sides of the equations:

$$\text{Oxidation: } 2H_2 \rightarrow 4H^+ + 4e^-$$

$$\text{Reduction: } 4H^+ + O_2 + 4e^- \rightarrow 2H_2O$$

$$2H_2 + O_2 \rightarrow 2H_2O + \text{energy}$$
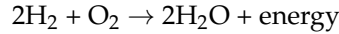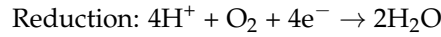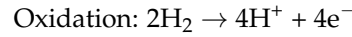
According to the fact that water (H_2O) is a liquid for temperatures below 100 °C and the chemical equation of the PEM fuel cell, the thermodynamic voltage equation would change for two different temperature ranges to Equation (1) [16]. In fact, P_{H_2O} exhibits the water activity between anode and electrolyte.

$$E_n = \begin{cases} E_0 + (T - T_0)\frac{\Delta S_0}{zF} + \frac{RT}{zF}\ln\left(P_{H_2}P_{O_2}^{\frac{1}{2}}\right) & T \leq 100\ °C \\[3mm] E_0 + (T - T_0)\frac{\Delta S_0}{zF} + \frac{RT}{zF}\ln\left(\frac{P_{H_2}P_{O_2}^{\frac{1}{2}}}{P_{H_2O}}\right) & T > 100\ °C \end{cases} \tag{1}$$

where F is the Faraday constant, z is the number of electrons transferred ($z = 2$), E_n is the thermodynamic voltage, E_0 is the standard electrode voltage, T_0 is the temperature at standard condition (298 K), and ΔS_0 exhibits the entropy of the chemical reaction (-44.43 J/mol K). The parameters of P_{H_2}, P_{O_2}, and P_{H_2O} denote the partial pressure of H_2, O_2, and H_2O in atm, respectively [17]. By substituting the aforementioned values in Equation (1), the Nernst equation can be obtained as follows [18]:

$$E_n = \begin{cases} 1.229 + (T - 298)\frac{-44.43}{zF} + \frac{RT}{zF}\ln\left(P_{H_2}P_{O_2}^{\frac{1}{2}}\right) & T \leq 100\ °C \\[3mm] 1.229 + (T - 298)\frac{-44.43}{zF} + \frac{RT}{zF}\ln\left(\frac{P_{H_2}P_{O_2}^{\frac{1}{2}}}{P_{H_2O}}\right) & T > 100\ °C \end{cases} \tag{2}$$

Assuming that the fuel contains $x\%$ hydrogen and the input air contains $y\%$ oxygen and $w\%$ water vapor, the partial pressures can be expressed based on the hydrogen and oxygen utilization as follows:

$$\begin{cases} P_{H_2} = \left(1 - U_{fH_2}\right)x\%P_{fuel} \\[3mm] P_{H_2O} = \left(w + 2y\%U_{fO_2}\right)P_{air} \\[3mm] P_{O_2} = \left(1 - U_{fO_2}\right)y\%P_{air} \end{cases} \tag{3}$$

where U_{fH_2} and U_{fO_2} are the values of hydrogen and oxygen utilization, respectively; these parameters can be calculated in terms of flow rate at the inlet, cell current, and pressures as follows [19]:

$$U_{fH_2} = \frac{6000 \times R \times T \times N \times i_{fc}}{2 \times F \times P_{fuel} \times V_{lpmf} \times x\%} \tag{4}$$

$$U_{fO_2} = \frac{6000 \times R \times T \times N \times i_{fc}}{4 \times F \times P_{air} \times V_{lpma} \times y\%} \tag{5}$$

where P_{fuel} and P_{air} are absolute supply pressures of hydrogen and air, respectively. The parameters V_{lpmf} and V_{lpma} are the flow rates of hydrogen and air at the inlet in L/min.

The fuel and airflow rates (FRs) are considered the inputs and are controlled by two separate regulators as follows [20]:

$$Fuel_{FR} = \frac{60000 \times R \times (273 + T) \times N \times I_{ref_{H_2}}}{2 \times F \times \left(101325 \times P_{f_{H_2}}\right) \times \left(\frac{U_{f_{H_2}}}{100}\right) \times \left(\frac{x_{H_2}}{100}\right)} \tag{6}$$

$$Air_{FR} = \frac{60000 \times R \times (273 + T) \times N \times I_{ref_{O_2}}}{4 \times F \times \left(101325 \times P_{f_{O_2}}\right) \times \left(\frac{U_{f_{O_2}}}{100}\right) \times \left(\frac{y_{O_2}}{100}\right)} \tag{7}$$

where U_{fH_2} and U_{fO_2} are nominal utilization of hydrogen (98.47%) and oxygen (35.2%), respectively. The parameters x_{H_2} and y_{O_2} are the composition of fuel (99.95%) and oxidant (21%), respectively, and I_{ref} is the reference current.

Fuel Cell Losses

Due to the losses that exist within the fuel cells, achieving the ideal cell potential is not possible, and the amount of voltage generated is always less than the theoretical value, which can be defined as voltage drop as shown in Equation (8):

$$V = E - E_{losses} \tag{8}$$

Typically, the losses occurring within a fuel cell can be divided into two main categories: ohmic polarization loss and activation loss. The main cause of the activation losses is the slow response of chemical reactions at the surface of electrodes. This group of fuel cell losses accounts for the most contribution to the total losses, which is why it is well-known as the most important factor in the voltage drop (V_{act}). A portion of the potential is consumed for emitting electrons to electrodes; therefore, it will reduce the total actual potential [21]. This means that the electrons are continuously moving which causes a current called the Exchange Current (i_0). The direct relationship between the exchange current and the activation voltage drop can be obtained by the electrochemical kinetics equation, and its simplified formula is shown in Equation (9) [22].

$$i_{fc} = i_0 e^{\frac{z\alpha F V_{act}}{RT}} \tag{9}$$

By taking the logarithm of both sides of the above equation, the activation voltage loss for the fuel cell can be determined as follows [23]:

$$V_{act} = -A \ln i_{fc} \tag{10}$$

$$A = \frac{RT}{z}\alpha F \tag{11}$$

$$V_{act} = \frac{RT}{z\alpha F} \ln\left(\frac{i_{fe}}{i_0}\right) = A \ln\left(\frac{i_{fe}}{i_0}\right) \tag{12}$$

where i_{fc} is the fuel cell current and A is the slope of the Tafel curve.

It should be noted that hydrogen oxidation at the anode is much faster than oxygen reduction at the cathode, and the cathode is the major factor in limiting the dynamic behavior of the activation voltage drop [24]. When the load suddenly changes, the amplitude of the current is directly proportional to the changes. These current variations instantaneously lead to altering the ohmic losses, but the cell voltage needs time to sense the changes and reaches its steady state. This problem can be solved by considering a delay based on the cell

response time (T_d) in the activation losses equation [25]. Therefore, the modified equation of the activation voltage drop can be found as follows:

$$V_{act} = \frac{RT}{z\alpha F} \ln\left(\frac{i_{fc}}{i_0}\right) e^{-sT_d} = \frac{RT}{z\alpha F} \ln\left(\frac{i_{fc}}{i_0}\right) \frac{1}{sT_d + 1} \tag{13}$$

In addition to the activation losses, another important loss is the ohmic or resistive loss, which is related to the transportation of protons and electrons within the cell. This loss is due to the resistance of the electrons in the anode and cathode and the resistance to the membrane. The total ohmic loss can be described by multiplying the current by an internal resistance (R_{ohm}) as follows:

$$V_{ohm} = V_{ohm.a} + V_{ohm.membrane} + V_{ohm.c} = I_{fc} \times R_{ohm} \tag{14}$$

The exchange current i_0 based on the hydrogen and oxygen concentration or partial pressures is derived as follows [26]:

$$i_0 = \frac{zFk\left(P_{H_2} + P_{O_2}\right)}{Rh} e^{\frac{-\Delta G}{RT}} \tag{15}$$

where k is the Boltzmann's constant and h is the Planck's constant.

When the current does not flow, the voltage will only depend on the inlet pressures because the utilization of hydrogen and oxygen is zero. For the currents greater than zero, the hydrogen and oxygen utilization will also affect the Nernst voltage. Thus, the open-circuit voltage would be as follows [19]:

$$E_{oc} = \begin{cases} K_i E_n & i_{fc} \leq 0 \\ \\ K_c E_n & i_{fc} > 0 \end{cases} \tag{16}$$

where K_i and K_c are the ratios of open circuit voltage to the Nernst voltage is zero and nominal hydrogen and oxygen utilization, respectively.

According to the mentioned equations, a detailed model of the PEM fuel cell can be extracted as shown in Figure 1. Additionally, the complete model is simulated in the MATLAB Simulink environment.
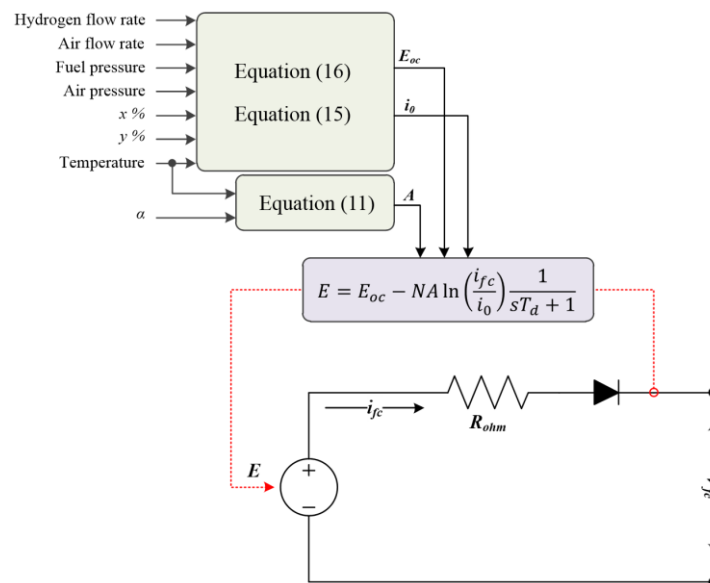
Figure 1. Block diagram of the overall equivalent circuit of the fuel cell.

The model used in this study has some limitations, such as neglecting the influence of temperature and humidity on the internal resistance or ignoring water and gases flow through the membrane [27]. In this detailed model, the following assumptions are made while simulating the PEM fuel cell [28]:

- The gases are ideal.
- The hydrogen and air are fed into the stack.
- The cooling system is embedded so that the temperature of the anode and cathode is stable at the stack temperature.
- A water management system is designed to adjust the humidity inside the cell to an appropriate degree under various conditions.
- Pressure drops across flow channels are ignorable.
- The cell resistance under any operation condition is considered to be constant.
- Considering that in most cases, the fuel cell does not operate in the mass transport region, the mass transport losses or concentration losses are negligible.

All the required parameters were modified based on the 25-kW used fuel cell as below:

- Nominal voltage: 210 V
- Nominal current: 120 A
- Number of cells: 300
- Nominal stack efficiency: 55%
- Operating temperature: 65 °C
- Fuel cell resistance: 0.487 Ω
- Nominal airflow rate: 2100 L/min

3. DC-DC Converters

DC-DC converters with step-up capability are widely utilized in a large number of industries and applications at different power levels from watts to multi-megawatts. Due to the ability of the converters to isolate the input from the output, they can be divided into two general categories: isolated and non-isolated. In power electronics, isolation means the electrical separation between the input and the output of a converter by using a transformer. The power converters in this category are mainly used in situations where more than one input is required [29]. However, these converters are not applicable in cases where a circuit with limited volume and weight is required. Therefore, the volume, weight, and transformer losses are the most important limiting factors for using these converters in embedded applications [30].

On the other hand, the non-isolated converters do not have a transformer in their structure, which will not only reduce the overall size of the converter but also reduce dissipated heat from switching and eliminate copper losses [31]. Another positive feature of a non-isolated converter is its low manufacturing cost which allows for operating at higher temperatures with higher efficiency [32].

3.1. Boost Converter

Boost converters are typically used to boost up the input voltage at the desired voltage level while stepping down the supply current. This converter is categorized as a switched-mode power supply and generally is composed of two semiconductor devices (diode/switching transistor) and storage elements (inductor/capacitor). The boost converter topology is shown in Figure 2.
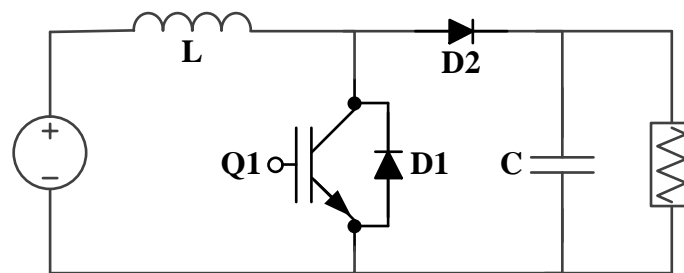
Figure 2. Circuit diagram of the conventional boost converter.

A controller is responsible for managing the switch between two states of "on" and "off". By flowing the current through the inductor during the on state, electrical energy is stored in the magnetic field; then, the capacitor supplies the current to load, and the diode is reverse-biased. During the off state, the diode is forward-biased and allows current to flow through the circuit; then, the stored energy will transfer to the load.

The boost converter can operate in both discontinuous conduction mode (DCM) and continuous conduction mode (CCM) which is determined by the effect on the current of the inductor [33]. In DCM, all energy stored in the inductor will be consumed in each cycle, there will be no energy and current for part of the time, and the inductor current will reach zero during a switching cycle. In CCM, the inductor current in each cycle is greater than zero, and some parts of the energy of each cycle remain to meet the next cycle. The usage of boost converters offers several benefits:

- Continuous input current
- Has the smallest possible number of components
- Simple drive circuit due to the grounded switch used in this topology

In contrast, this converter has some drawbacks such as [34]:

- Requiring a large capacitor size
- Poor efficiency for very large duty cycles
- Non-isolated input from the output
- High switching noise

The input and output voltages in the boost converter have a direct relationship with the duty cycle of the pulses which can be described as follows:

$$\frac{V_{out}}{V_{in}} = \frac{1}{1 - D} \tag{17}$$

where V_{out}, V_{in}, and D are the output voltage of the converter, the input voltage, and the converter's duty cycle, respectively. Regarding the value of $0 < D < 1$, it is clear that the output voltage is always higher than the input voltage.

For converters that have a high current output, the use of a switch instead of a diode in the output looks quite reasonable. Synchronizing in the power converters means replacing the switch instead of the diode; and here, a synchronous boost converter with two switches is considered for analysis. In cases where the large voltage drop across the diode is not desirable, a synchronous converter can be used to improve efficiency and power losses. If the current level stays the same in both synchronous and non-synchronous topologies, the voltage drop of the switch will be less than the diode, resulting in lower power dissipation and heat generated in the semiconductor [35]. For duty cycles of more than 40%, the efficiency of a synchronous boost converter would be greater than non-synchronous [36]. However, ideal semiconductor devices are considered in this paper, and the power losses and temperatures of this topology would not be different with the nonsynchronous boost converter.

3.2. Interleaved Boost Converter

As mentioned earlier, one of the major disadvantages of the conventional boost converter is operating at a high duty cycle ratio which leads to reducing efficiency, increasing switching losses, and a high voltage drops over the parasitic elements [37]. By proposing the interleaved boost converter, different benefits—such as reduced input-output ripple, higher efficiency, and improved reliability—are realized while using this topology [38]. Furthermore, using the interleaved boost converter would be associated with smaller parasitic elements, which reduces the power losses in the circuit. Here, a two-phase interleaved boost converter, as illustrated in Figure 3, is considered.
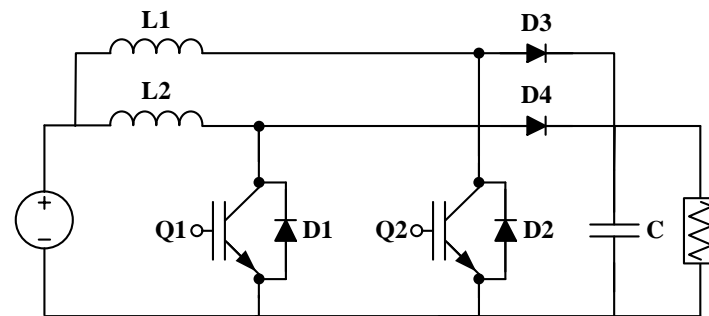
Figure 3. Circuit diagram of the interleaved boost converter.

Due to the two-phase structure of this converter, each phase must operate at 180° according to the phase shift equation. Considering the simultaneous operating of these two phases, the frequency of the whole circuit is doubled which can reduce the voltage ripple. Additionally, the input current ripple decreases by increasing the frequency. During the on state for the first phase, the inductor current increases and it will store energy in the inductor; but during the off state, this stored energy will be delivered to the load through the first phase. By giving the gate pulse to the second phase, a similar process to the first phase will be performed to store and discharge energy in the inductor [39]. Therefore, these two phases alternately feed the load. The voltage conversion ratio is similar to the conventional boost converter, but the duty cycles should be carefully selected so that they do not overlap [40].

3.3. Floating Interleaved Boost Converter

Another topology examined in this paper is a floating interleaved boost converter which is a mixture of two boost converters at the same input and output. This topology is shown in Figure 4.
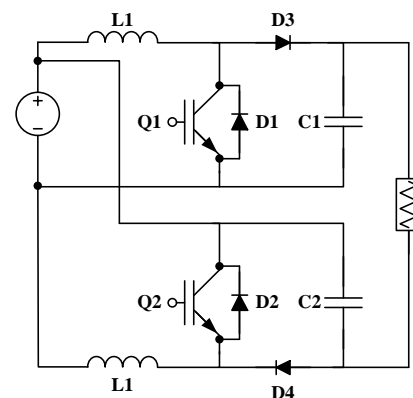
Figure 4. Circuit diagram of the floating interleaved boost converter.

This two-stage converter is able to operate in lower current and voltage ripples resulting in an increased rating for the converter. According to the literature [41], the advantages of the floating interleaved boost converter over the basic topology are as follows:

- Higher efficiency
- Higher voltage ratio for the converter
- Higher input and output frequency—fewer losses
- Improved reliability due to the parallel structure
- Reduced size of the parasitic elements, weight, and volume

During various modes of operation, the two output capacitors always have a series connection with the voltage source. The relationship between the input and output voltages is as follows [42]:

$$\frac{V_{out}}{V_{in}} = \frac{1 + D}{1 - D} \tag{18}$$

As is evident, to achieve the same output voltage level in the floating boost converter, a lower duty cycle is required compared to the conventional boost converter. This means this topology is able to provide a higher gain than the basic boost.

3.4. Multi-Switch Boost Converter

For high power applications, one of the ways to circumvent thermal damage from semiconductor devices in a basic converter topology is paralleling several power semiconductors (or switches) when a single switch is not able to handle the flowing current. This means the high current that passes through a single switch and causes a sharp rise in its temperature can be divided into two or more portions in a multi-switch topology. This method can be adopted when the basic boost converter is suffering high power dissipation, has an inability to control high currents, thermal management issues, or magnetic design [43]. A dual-switch boost converter is shown in Figure 5.
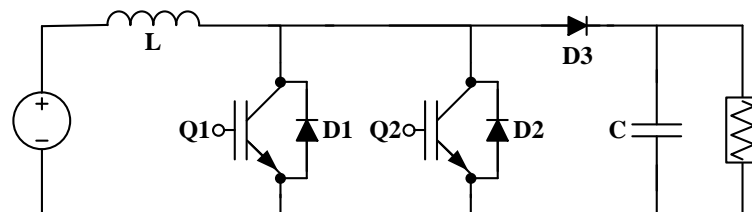
Figure 5. Circuit diagram of the multi-switch boost converter.

It is clear from Figure 5 that it would not be reasonable if the two switches were turned on simultaneously. For this reason, the entire duty cycle of a basic boost topology should be divided between the two switches equally or unequally. In this study, the duty cycle is evenly divided between two switches (i.e., each switch is responsible for 25% of the cycle). Therefore, in order to avoid overlapping, the duty cycle of the second switch should be applied with a delay of 1/4 cycle compared to the first switch.

3.5. Cuk Converter

Cuk converter is another basic DC-DC converter which is a series combination of boost and buck converters. This feature allows us to adjust the output voltage to greater or less than its supply voltage. However, this converter also has the same drawback as the buck-boost converter, which denotes its output polarity is always negative while operating in the CCM mode. The diode would be reverse-biased when the switch is turned on, and the inductors' current would increase; this means the power can be delivered to the output load. The diode would be forward-biased when the switch is off, and it leads to the charging of the coupling capacitor. Thus, the output voltage conversion ratio for the Cuk converter is as follows:

$$\frac{V_{out}}{V_{in}} = \frac{D}{1 - D} \tag{19}$$

This topology can offer some benefits such as higher efficiency, less current ripple, and reduced switching losses over the buck-boost topology [44]. In order to provide a

positive output voltage, an extra diode and an extra switch can be added to the conventional topology, as shown in Figure 6 [45]. The voltage conversion ratio would be the same as the inverting Cuk converter. This single-stage topology operates based on the charging and discharging of the capacitor located in the middle [46].
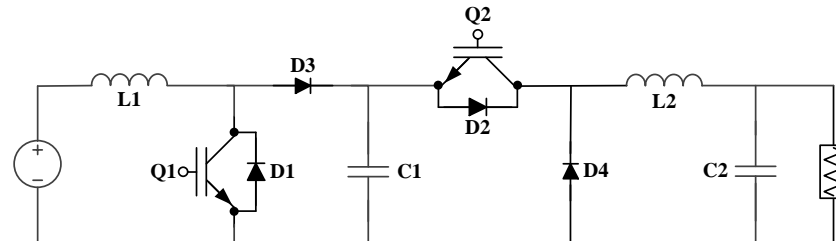
Figure 6. Circuit diagram of the Cuk converter.

4. Thermal Model of Power Semiconductors

Over recent years, system design requirements and reliability issues related to the thermal analysis of power electronic converters have been placed at the top of the priority list. Thus, an accurate approach for determining and simulating the thermal behavior of power semiconductors utilized within a power converter seems to be crucial; and the key to achieving optimal performance and increasing the lifespan of the converter is to determine the junction temperature. Due to the large time constant and delayed response of the heatsink (or cooling system) relative to the temperature, direct measurement of the junction temperature from these available points is subject to a great deal of error. Nevertheless, a method for proper temperature estimation should be provided. This method mainly involves thermal modeling of both semiconductor devices and cooling systems by assuming the thermal resistances and capacitances; then, applying the power losses as the input to this model and the output would be equal to the junction temperature. Therefore, the first step for estimating the temperature is adopting a method of power loss estimation in a power module.

Types of power semiconductors' losses are mainly divided into two categories: conduction and switching losses. The IGBT switch is not ideal and has an internal resistance, which is why a voltage will be caused by conducting the current. The conduction losses can be calculated by multiplying the instantaneous-collector current (I_c) by the on-state collector-emitter voltage (V_{ce}) as follows [47]:

$$P_{con} = I_c \times V_{ce}(I_c, \, T_j) \tag{20}$$

The voltage V_{ce} at the same time depends on both the collector current and the junction temperature (T_j); thus, at each step, the temperature of the previous step should be determined for calculation. The voltage, current, and junction temperature relationships are presented as a line graph in the product's datasheet. Given that this graph is only provided for a limited number of temperatures (e.g., 25 °C and 125 °C), linear interpolation and extrapolation should be employed for the rest of the temperatures between and outside the given two temperatures. The whole process will be implemented by the lookup table method as a measurement-based method. The conduction losses of the diode can be extracted by substituting the diode forward voltage (V_f) and the current in a forward-biased state (I_f) with the aforementioned parameters.

The switching losses in an IGBT can be defined as the losses due to the charging and discharging of the internal capacitance while fast turning off and on. The switching losses can be determined by multiplying the switching frequency (f_{sw}) by the energy losses in each commutation, where this energy loss is a function of the supply voltage (V_{cc}) and the collector current (I_c) as follows [47]:

$$P_{sw} = (E_{on}(V_{cc}, \, I_c, \, T_j) + E_{off}(V_{cc}, \, I_c, \, T_j)) \times f_{sw} \tag{21}$$

Meanwhile, this type of loss is also directly dependent on the junction temperature, and by raising the temperature, it will increase. For this reason, similar to the conductive losses, the lookup table method is also required for calculating switching losses, but with the difference that the interpolation should also be used for the supply voltage and junction temperatures. It is evident that by increasing the switching frequency, the switching losses will also rise. The mentioned procedure should be repeated for the diode's losses by using reverse recovery energy loss (E_{rr}) instead of the summation of on-off energy losses [47].

Power losses play the role of a heat source for the thermal modeling of an IGBT module. If the power loss inside the module is so high, an extreme junction temperature will be produced which can cause severe damage to the component. Thus, the junction temperature (T_j) should always be kept below the maximum allowable value. In addition, the temperature swing (ΔT_j), maximum (T_{jmax}), and minimum (T_{jmin}) temperatures are also important factors for failure [48]. Mechanical failures occur when the power semiconductor has experienced a specified number of thermal cycles, which will be discussed more in detail at a later moment. Therefore, the thermal model should also be able to determine the temperature fluctuations precisely.

There are different approaches for estimating the junction temperatures such as the finite elements method (FEM) and thermal equivalent circuits [49]. Resistance-Capacitance (RC) thermal model is the most popular way of estimating temperature due to its simplicity and considerable accuracy. This flexible model was first introduced in 1959 [50], and today it can be used for 1-D, 2-D, and 3-D modeling. The RC thermal model is usually defined by two types: Foster and Cauer. Although the Foster model does not provide a physical concept, it is easy and possible to transform this model into the same-order Cauer model by solving mathematical equations [51]. In this study, a Cauer ladder network is considered for the junction-to-case section. In order to implement an IGBT/diode into this thermal model, it is required to represent the heat conduction path from the upper layer (junction) to the lowest layer (case); then, it is needed to continue this heat flux path from the case to the ambient through a heatsink. Due to the similarity of the electro-thermal model, power losses would be considered as a continuous current source in the RC thermal model. This process is depicted in Figure 7.
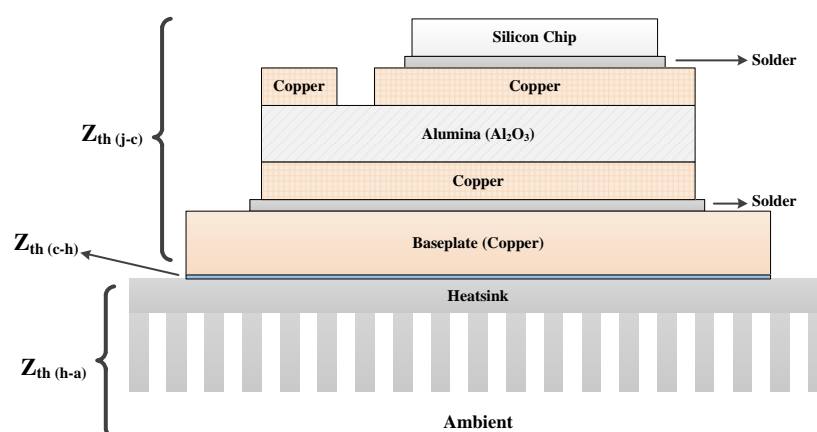
Figure 7. Cross−sectional representation of IGBT power module.

It is evident that there are different layers with various materials and physical dimensions from junction to case, and one RC-pair is assigned to each layer based on the layer's thickness, thermal conductivity, effective area, specific heat, and density. Moreover, physical modeling in the simulation environment can be used to display the heat transfer between the case and the ambient, so that the case-to-heatsink and heatsink-to-ambient thermal transfers are conduction and convective, respectively. More detailed explanations of the implemented physical model are provided in [47]. Due to the dependence of the power dissipations on the temperature, computations must be made as a closed recursive loop, as shown in Figure 8.
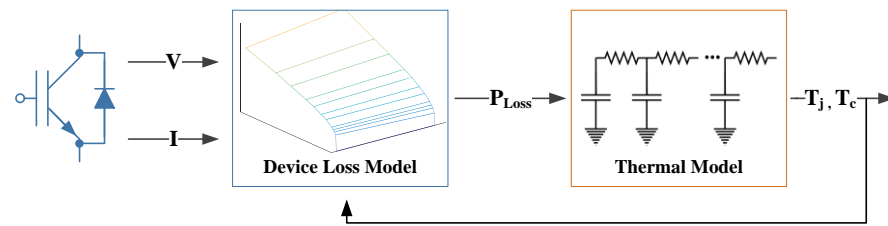
Figure 8. Closed recursive loop for determining the semiconductors' junction temperature.

5. Reliability Evaluation

The switching devices used in power electronic converters are the most failure-prone components and they are easily damaged. As power modules are composed of different layers with various thicknesses, materials, and physical properties, the thermal expansion for each layer will show a different behavior over a given temperature. Thus, the power module is subject to failure due to this thermal stress caused within its structure. For this reason, methods such as thermal cycling are enormously useful in identifying degradation mechanisms that dominate the lifetime of power modules [52]. The thermal stress will gradually lead to fatigue and the useful life of the module will be the same as the number of thermal cycles, which reduces with increasing junction temperature's fluctuation. Power cycling is an efficient method for subjecting the bonded connections, soldered joints, and substrate lamination to thermal cycling [53]. During the power cycling test, the power semiconductors are repeatedly heated up by the power losses inside the module; then, they are cooled down by the cooling system. The cycle length is usually between several milliseconds to a few seconds [54].

There are various analytical methods to link the failure mechanism to reliability performance, and by using these methods, an accurate prediction of the module lifetime would be expected. The most well-known lifetime model is the Coffin–Manson model, which is a strain-based model. The Coffin–Manson model is presented as follows:

$$N_f = \alpha \left(\Delta T_j \right)^{-n} \tag{22}$$

where α and n are constant parameters that are empirically obtained. This simple equation simply indicates that the number of cycles to failure is directly related to the temperature change (ΔT_j). The parameter of ΔT_j shows the difference between the maximum and minimum temperatures for each cycle. In [55], it has been concluded that the average junction temperature also affects the lifetime and must be included in the aforesaid equation (Equation (22)). Thus, the Coffin–Manson model was modified by the Arrhenius approach as follows [55]:

$$N_f = \alpha \left(\Delta T_j \right)^{-n} \exp\left(\frac{E_a}{k_b T_{jm}} \right) \tag{23}$$

where T_{jm}, E_a, and k_b are the average junction temperature (in Kelvin), activation energy, and Boltzmann constant (8.617×10^{-5} eV/K), respectively. Another analytical lifetime model is known as Norris—Landzberg model, which also considers the frequency of temperature cycles. The equation related to the Norris–Landzberg model is given in the following equation [56]:

$$N_f = \alpha \times f^{n_2} \times \left(\Delta T_j \right)^{-n_1} \exp\left(\frac{E_a}{k_b T_{jm}} \right) \tag{24}$$

If the frequency of the temperature cycle is 1 Hz, this model will be the same as the improved Coffin–Manson model (Equation (23)). It should be noted that all parameters of a Coffin–Manson model must be characterized prior to employment, according to the structure of the desirable power module. To obtain the model parameters, the power cycling capability diagram provided in the datasheet should be used. Since the Fuji U-

series power module is utilized in this paper, the power cycling diagram for this module is shown in Figure 9.
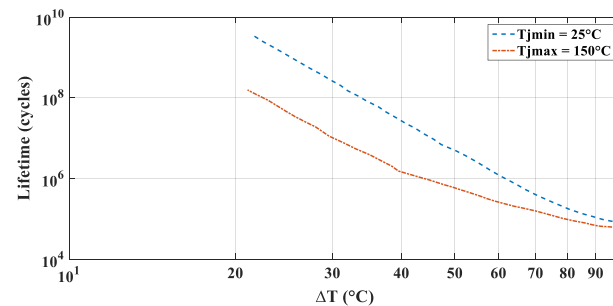
Figure 9. Power cycling lifetime curve for the Fuji U-series IGBT module.

Here, the curve fitting toolbox in MATLAB is used to extract the lifetime model's parameters. The obtained parameters for the examined power module are calculated as $\alpha = 3.128 \times 10^{12}$, $n = 4.326$, and $E_a = 0.06606$ eV. To neglect the effect of cycling frequency in the lifetime model, the input power would be in the form of a square pulse (heating 0.5 s and cooling 0.5 s) as shown in Figure 10.
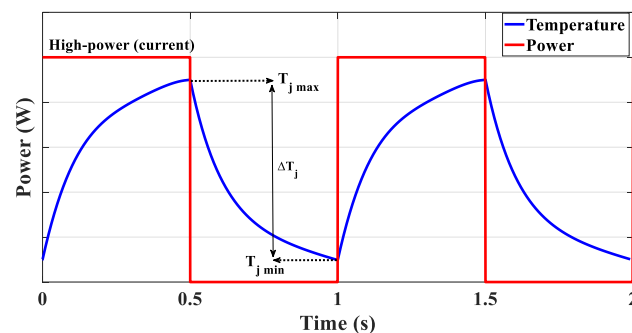
Figure 10. IGBT temperature variations under power cycling test.

6. Results and Discussion

The obtained results from the thermal analysis of the examined converters are presented in this section. In the first part, a comparison will be made between the studied converters from the point of view of thermal behavior and temperature variations. In the second part, by performing a thermal cycling simulation, a comparative analysis will be done in terms of reliability. In the last part, the rating of converters will be presented in terms of different indicators such as the thermal behavior, reliability, number of components, and cost.

6.1. Conventional Boost Converter

The thermal behavior of different components within the boost converter is provided in Figure 11. It can be seen that the junction temperatures start to rise from the ambient temperature (25 °C), and after 1 s, they almost reach their constant values in accordance with the fixed output load. It should be noted that the diode chips always have smaller cross-sectional areas and higher thermal resistance; thus, at the same power losses, the diode would have a higher temperature than an IGBT switch.
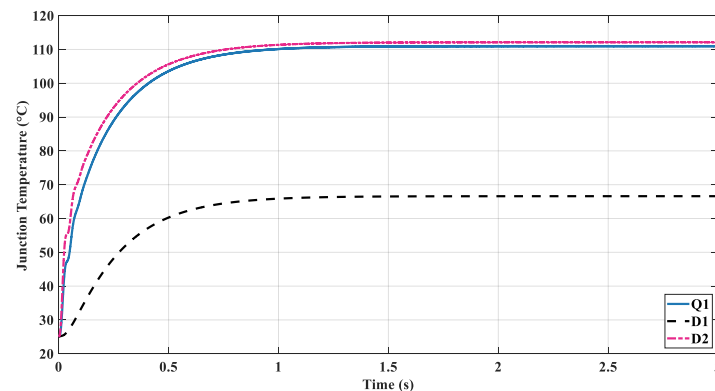
Figure 11. The junction temperature of the power semiconductors within the conventional boost converter.

The lowest temperature rise is related to the anti-parallel diode (D1) which has a temperature increase of about 41 °C. Here, the steady-state junction temperature for the switch is undesirably high while supplying an output power of 25 kW, and its final temperature rises to approximately 110 °C. Although this converter has a quite simple topology with only three semiconductor devices in its structure, its components' temperature seems not to be entirely compatible with the fuel cell applications.

6.2. Interleaved Boost Converter

Due to the aforesaid advantages of this converter compared to the conventional boost converter, the interleaved topology has achieved a good reputation as a step-up converter in fuel cell systems. The junction temperatures related to the semiconductors used within this topology are shown in Figure 12.
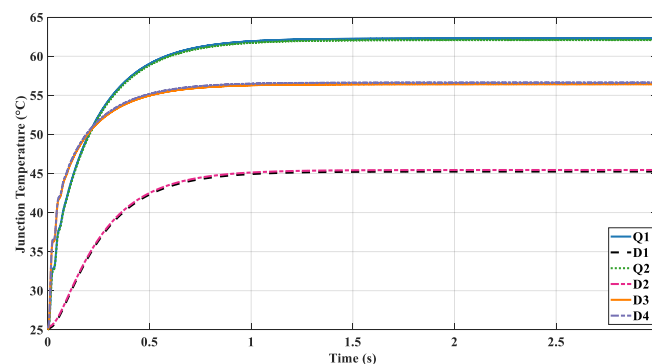
Figure 12. The junction temperature of the power semiconductors within the interleaved boost converter.

As is evident from Figure 12, the temperatures in each pair are similar (Q1 = Q2, D1 = D2, and D3 = D4) because of the symmetrical structure of the converter topology. Among the semiconductor devices, the junction temperature of Q1 and Q2 is the highest (62.28). While the D1 and D2's junction temperature rise is only 20.45 °C, the diodes D3 and D4 experience considerable thermal stress leading to an increased temperature to 56.62 °C.

6.3. Floating Interleaved Boost Converter

The semiconductor devices of this converter will have the same thermal behavior due to the symmetric structure (Q1 = Q2, D1 = D2, and D3 = D4). Due to multiple benefits of this converter (e.g., low input current ripple), it is very suitable for fuel cell applications. In addition, by increasing the number of stages in this structure, the overall performance of this converter would be improved; however, adding each floor increases the cost and complexity. The results of the thermal analysis are provided in Figure 13.
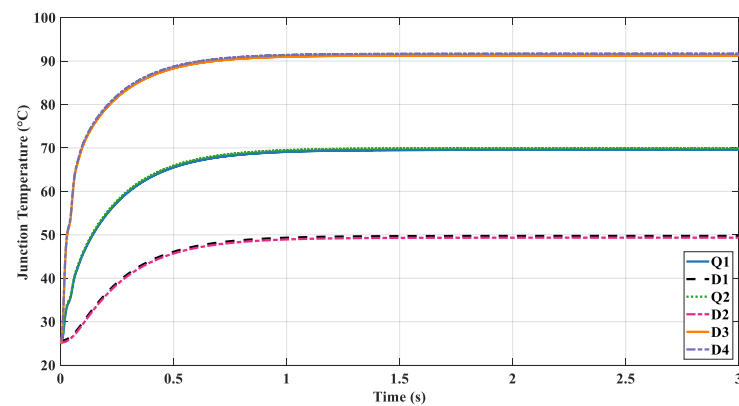
Figure 13. The junction temperature of the power semiconductors within the floating-interleaved boost converter.

In this converter, the most dominant heat source is the diode D3 (or D4), which operates at a temperature of 91.66 °C. The switches also work at an operating temperature of 69.57 °C, which is much lower than the conventional boost converter. This obvious temperature reduction is also repeated for the diode, and the anti-parallel diode's temperature is only about 49 °C.

6.4. Multi-Switch Boost Converter

The main purpose of this topology is to divide the thermal stress created on one single pair of switch/diode into several parallel pairs. Therefore, although the number of used components will increase, the average thermal stress will be lowered. The components' temperature variations are illustrated in Figure 14.
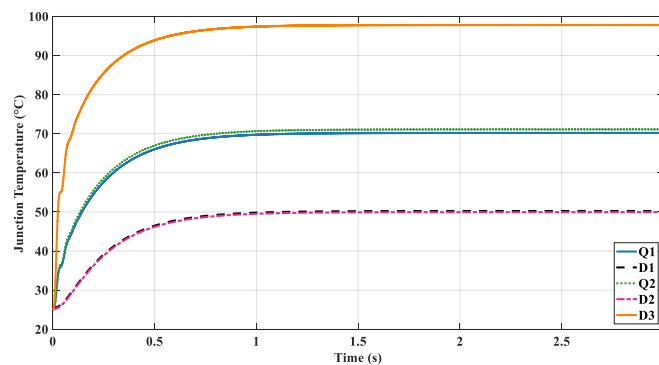
Figure 14. The junction temperature of the power semiconductors within the multi-switch boost converter.

As it is clear from Figure 14, this topology has been able to greatly reduce the temperature of the switches so that the junction temperature drops from 110 °C for the switch utilized in the conventional boost converter to 70.21 °C by the equalization of the thermal stress on two parallel switches. Because the duty cycle is divided equally between the two switches, their temperature behavior would be the same during the operation. Additionally, this topology is capable of reducing all diodes' temperature—the anti-parallel diode from 66.60 to 49.93 °C and D3 from 112.11 to 97.83 °C.

6.5. Cuk Converter

According to this topology, it is expected that the most flowing current is related to the switch Q1 and the diode D2. This current passing through these semiconductor devices can cause a tremendous amount of power loss and generated heat. The results are depicted in Figure 15.
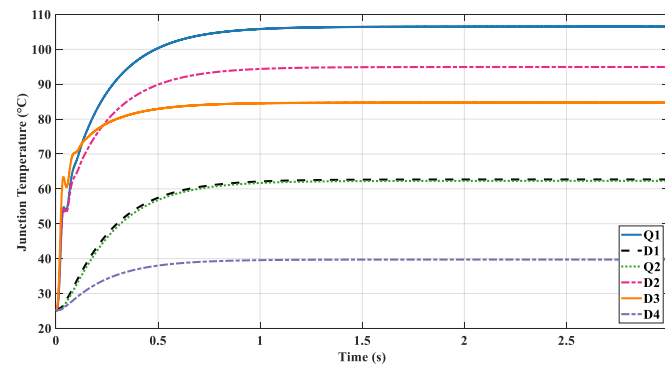
Figure 15. The junction temperature of the power semiconductors within the Cuk converter.

As depicted in Figure 15, the switch Q1 with a junction temperature of 106.5 °C is the hottest component in this converter. The temperature of the diode D2 is also ranked second with 94.94 °C after switch Q1, which has the highest power loss/temperature among the diodes. The interesting thing about this topology is that the switch Q2 and the anti-parallel diode D1 are experiencing the same junction temperature which is equal to 62.29 °C. The diode D4 has the smallest contribution to reducing the reliability and lifespan because while operating, its temperature has only a slight increase from the ambient temperature (approximately 15 °C).

6.6. Reliability Assessment

According to prior studies, semiconductor devices used in power electronic converters have always been considered a major factor in reducing reliability and lifetime [57]. Thus, the reliability of the most fragile components of the system has been evaluated in the first stage while undertaking lifetime assessments. To analyze the semiconductor devices in terms of reliability, the above-mentioned relationships are used, and a thermal cycling test must be performed on the converters under study. The extracted results of this simulation on the boost converter are shown in Figure 16.
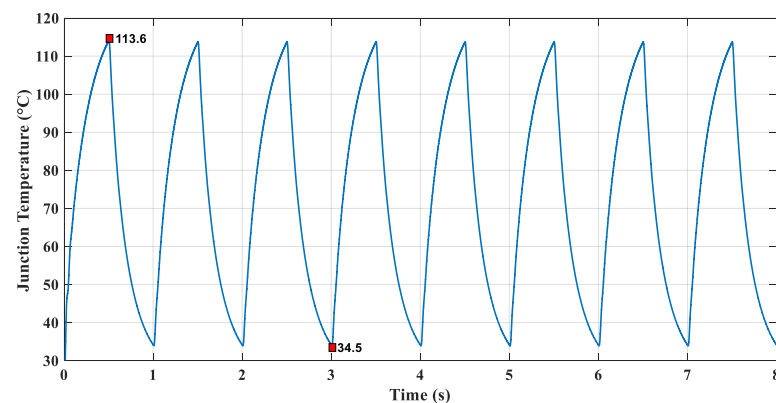
Figure 16. The temperature variations of the IGBT used in the boost converter during the power cycling test.

As is clear from Figure 16, a constant power has been applied to the power module in the first part of the cycle (0.5 s), and in the next 0.5 s, the applied power to the semiconductor devices is interrupted and the module is allowed to cool down by the heatsink (or cooling system). During this test, depending on the cooling capacity of the heatsink, the junction temperature may reach the ambient temperature over the cooling phase or may not. For instance, in the boost converter case, the junction temperature did not reach the ambient temperature (25 °C).

What is important from this test for reliability analysis is the maximum and minimum temperatures during the thermal cycling, as the lifetime of the module is also measured by these values (these maximum and minimum values are specified in Figure 16). To determine the parameters ΔT_j and T_{jm}, these maximum and minimum temperatures are adequate; then, by performing the thermal test for all the converters under the mentioned conditions, the data listed in Table 1 can be found. Therefore, the Norris–Landzberg parameter (the number of cycles) can be calculated by substituting values in Equation (24).

Table 1. The obtained results from the power cycling test for all five converters.

Converters	T_{jmax} (°C)	T_{jmin} (°C)	T_{jm} (°C)	ΔT_j (°C)	N_f (No. Cycles)
Conventional Boost	113.60	34.47	74.04	79.13	174,568
Interleaved Boost	65.41	29.44	47.43	35.97	6,350,411
Floating Interleaved Boost	58.72	29.20	43.96	29.52	15,325,855
Multi-switch Boost	65.87	28.89	47.38	36.98	5,635,353
Cuk	99.87	31.52	65.70	68.35	347,316

It is clear from Table 1 that the conventional boost converter is quite failure-prone due to its improper performance in terms of reliability. In the meanwhile, the most competitive topologies are interleaved, floating interleaved, and multi-switch. Although there seems to be no significant temperature difference between these converters, the number of cycles can vary enormously even with a slight difference in temperature values, so the floating interleaved converter has almost three times better performance than the interleaved converter.

In order to have a better comparison between the studied converters, it is necessary to examine all indicators related to thermal performance, reliability, number of components, and cost at the same time. The first important factor in choosing the best converter for fuel cell applications is the number of cycles, because a higher number of cycles means a greater useful lifespan.

The second most important factor among the chosen topologies is the highest junction temperature among the semiconductor devices ($T_{jmax(Q)}$ and $T_{jmax(D)}$); these values need to be as low as possible for more efficient operation and an optimal cooling system. The diodes and IGBTs corresponding to the highest temperature are specified for each converter as follows:

- Conventional Boost: D2 and Q1
- Interleaved Boost: D3 (or D4) and Q1 (or Q2)
- Floating Interleaved Boost: D3 (or D4) and Q1 (or Q2)
- Multi-switch Boost: D3 and Q2
- Cuk: D2 and Q1

The next decisive factor in a fuel cell system is the cost of the converter, which is even preferred in some cases to the performance. To determine the cost indicator, four different levels are specified: very low (1), low (2), average (3), and high (4). The next factor is the number of circuit components; a smaller number of components would be better. Reducing the number of circuit components—particularly power switching devices and the required drive circuit—is important because it reduces the weight, size, cost, and installation area [58]. The aforesaid indicators are given in Table 2. In the next step, a ranking methodology should be proposed that can be applied to the information provided in Table 2.

Table 2. The selected criteria and information for the ranking procedure.

Converters	N_f(No. Cycles)	$T_{jmax\ (Q)}$ (°C)	$T_{jmax\ (D)}$ (°C)	No. Components	Cost
Conventional Boost	174,568	111.00	112.10	5	Very Low
Interleaved Boost	6,350,411	69.94	91.66	9	High
Floating Interleaved Boost	15,325,855	62.25	56.65	10	High
Multi-switch Boost	5,635,353	71.12	97.76	7	Average
Cuk	347,316	106.50	94.94	10	High

The Technique for Order Preference by Similarity to Ideal Solution (TOPSIS) method [59], which is one of the most popular approaches for decision making, has been used to allocate a rank for each topology. In the TOPSIS method, the ideal (positive) solution is the one that maximizes the benefit of the criteria/attributes and minimizes the cost of the criteria (attributes), while the negative ideal solution is the one that maximizes the cost of criteria/attributes and maximizes profit criteria (attributes). The closest alternative to the ideal solution and, at the same time, the farthest from the negative ideal is the best alternative. In the TOPSIS method, the following procedure must be followed [60]:

1. Calculate the normalized decision matrix $\overline{X}_{ij} = [x_{ij}]_{m \times n}$ based on the normalized values as follows:

$$\overline{X}_{ij} = \frac{x_{ij}}{\sqrt{\sum_{j=1}^{n} x_{ij}^2}} \tag{25}$$

2. Calculate the weighted normalized decision matrix by multiplying the selected weights by the normalized values as follows:

$$V_{ij} = \overline{X}_{ij} \times W_j \tag{26}$$

In this step, a weight should be considered for each criterion. A greater weight of the criterion shows that it is more important in the overall utility compared with criteria with lower weights. The weights are usually normalized so that their summation would be equal to 1 [61].

3 Determine the positive and negative ideal solutions:

$$\begin{aligned} V^+ &= (V_1^+, V_2^+, \dots, V_n^+) \\ V^- &= (V_1^-, V_2^-, \dots, V_n^-) \end{aligned} \tag{27}$$

where,

$$V_j^+ = \begin{cases} \max_i(V_{ij}) & \text{if criterion } j \text{ is benefit} \\ \\ \min_i(V_{ij}) & \text{if criterion } j \text{ is cost} \end{cases}$$

$$V_j^- = \begin{cases} \min_i(V_{ij}) & \text{if criterion } j \text{ is benefit} \\ \\ \max_i(V_{ij}) & \text{if criterion } j \text{ is cost} \end{cases} \tag{28}$$

In this analysis, the Norris–Landzberg parameter (N_f) is only considered as a benefit, while all other indicators are non-beneficial criteria (cost).

4 Calculate the distance of each alternative from the ideal solution by using the Euclidean distance formula as follows:

$$S_i^+ = \sqrt{\sum_{j=1}^{m} (V_{ij} - V_j^+)^2} \tag{29}$$

Similarly, the Euclidean distance from the negative ideal solution can be obtained by:

$$S_i^- = \sqrt{\sum_{j=1}^{m} \left(V_{ij} - V_j^-\right)^2} \tag{30}$$

5   Calculate the relative closeness for each alternative as the performance score by dividing its positive ideal solution by the summation of its ideal solutions:

$$P_i = S_i^- / (S_i^- + S_i^+) \tag{31}$$

A higher value of the closeness coefficient indicates that the alternative is closer to the positive ideal solution. Thus, in the final stage, the alternatives must be ranked based on the calculated relative closeness that will make the alternative perform the best. In this research, the considered weights for the Norris–Landzberg parameter (N_f) for the maximum junction temperature of switches ($T_{jmax(Q)}$), maximum junction temperature of diodes ($T_{jmax(D)}$), number of total components, and cost are 0.2, 0.2, 0.2, 0.1, and 0.3, respectively. From these selected weights, it is clear that the total cost is more significant compared to a single lifetime criterion, but by assuming all three reliability factors, these reliability indicators will play a critical role in selecting the most proper topology. In the meantime, the number of circuit components is important because it influences the size, weight, and complexity of the circuit. The above procedure has been implemented in a MATLAB environment in which the obtained closeness coefficients (or performance score) and ranks are listed in Table 3.

Table 3. The determined performance scores and ranks for the candidates (first scenario).

Converters	Performance Score (*P*)	Rank
Conventional Boost	0.3306	4
Interleaved Boost	0.3553	3
Floating Interleaved Boost	0.6694	1
Multi-switch Boost	0.3679	2
Cuk	0.1092	5

As can be seen from Table 3, the best ranking is by far related to the floating interleaved converter because this converter performs the best in terms of both reliability and thermal behavior. Interestingly, the conventional boost converter is ranked fourth by considering the factors such as the number of components, simplicity, and cost. Although the cost is significantly important, this converter could not gain a high-performance score. The multi-switch converter is in the second place due to its superiority (less cost and number of components) to the interleaved converter. The Cuk converter also gets the worst rating and comes in the last place, with a performance score of 0.11.

To clarify that if the overall performance (reliability and thermal conditions) is the highest-priority indicator rather than the cost, another scenario is considered here in which it is assumed that the cost weight is 0.2 instead of 0.3; and the Norris–Landzberg parameter weight increases from 0.2 to 0.3. The rest of the weights remain unchanged. The newly generated data according to the assigned weights are presented in Table 4.

Table 4. The determined performance scores and ranks for the candidates (second scenario).

Converters	Performance Score (*P*)	Rank
Conventional Boost	0.2631	4
Interleaved Boost	0.3782	2
Floating Interleaved Boost	0.7369	1
Multi-switch Boost	0.3690	3
Cuk	0.0579	5

In this scenario, it is evident that all the scores have become completely different so that the interleaved converter moved to second place. The multi-switch converter is in third place, ahead of the conventional boost. The Cuk converter has the lowest performance score and is still in the last place, as expected. Considering that the number of cycles is always known as a crucial factor in determining the suitable converter for the fuel cell systems, the floating interleaved converter will not lose its place at the top of the list. When evaluating the outcomes from these two different scenarios, from a practical viewpoint, it is worth mentioning that the weight of each indicator should be chosen based on the requirements of the system designer.

7. Conclusions

Despite significant efforts to design several DC-DC converter topologies appropriate for fuel cell applications, there is a paucity of thorough research on the reliability and thermal performance of these converters. This paper presented an in-depth thermal and reliability analysis of five commonly used DC-DC boost converters in fuel cell systems. The thermal analysis was performed based on determining semiconductor devices' junction temperature via a thermal network model. Then, a power cycling test was done by applying a periodic power (with a frequency of 1 Hz) on the semiconductors so as to calculate the number of cycles to failure as the most critical indicator in reliability assessment. The results showed that the conventional boost converter (with a maximum IGBT junction temperature of ~110 °C) has the weakest thermal performance among the studied converters. The switching devices in the Cuk converter were also likewise subjected to significant thermal stress. In contrast, the floating interleaved boost converter was able to get the first rank in terms of thermal performance, and a temperature of ~62 °C was recorded for the IGBTs used in this converter. In terms of reliability, the conventional boost converter remains the least reliable (with N_f ~ 174k cycles), while the floating interleaved boost converter is likewise the most reliable choice. The interleaved boost converter has also demonstrated remarkable lifespan performance, ranking second (N_f ~ 6300k cycles). The analysis, including both thermal/reliability aspects, revealed that the floating interleaved boost converter performs much better compared to the conventional boost and other considered topologies.

To observe the effect of other indicators (i.e., the number of circuit components and cost), a ranking methodology named TOPSIS has been used to arrange the converters according to their overall performance score. In the first scenario, the weights taken into account for the reliability indicator, maximum IGBTs' temperature, maximum diodes' temperature, number of total components in the circuit, and cost which were 0.2, 0.2, 0.2, 0.1, and 0.3, respectively. The cost weight was assumed to be predominant in this scenario. The findings of this scenario revealed that the floating interleaved boost converter rated best in terms of overall performance, whereas the Cuk converter ranked worst when several indications were considered. Additionally, a second scenario was considered in which, unlike the first scenario, the reliability indicator (0.3) was more important than the cost (0.2). By considering a greater weight (0.3) for the cost criterion than the reliability (0.2), the conventional boost converter ranked fourth among the examined converters. In addition, the results showed that the floating interleaved boost converter would be the most proper choice for fuel cell applications as it is always at the top of the list in different scenarios (performance scores of 0.67 and 0.74 for the two chosen scenarios, respectively), while the poorest results have been found in the Cuk converter in both scenarios. Evaluation of other proposed topologies (e.g., Z-source converter) for fuel cells in terms of reliability and thermal performance should be considered as a future study.

Author Contributions: Conceptualization, O.A. and M.D.; methodology, O.A.; software, O.A. and M.D.; validation, O.A.; formal analysis, O.A., T.R., W.D.C. and M.D.; investigation, O.A. and M.D.; resources, T.R., W.D.C. and M.D.; data curation, M.D.; writing—original draft preparation, O.A.; writing—review and editing, T.R., W.D.C. and M.D.; visualization, O.A.; supervision, W.D.C. and M.D.; project administration, M.D.; funding acquisition, M.D. All authors have read and agreed to the published version of the manuscript.

Institutional Review Board Statement: Not applicable.

Informed Consent Statement: Not applicable.

Data Availability Statement: Not applicable.

Conflicts of Interest: The authors declare no conflict of interest.

References

1. Rajabloo, T.; De Ceuninck, W.; Van Wortswinkel, L.; Rezakazemi, M.; Aminabhavi, T. Environmental management of industrial decarbonization with focus on chemical sectors: A review. *J. Environ. Manag.* **2022**, *302*, 114055. [CrossRef]
2. Andujar, J.M.; Segura, F.; Vasallo, M.J. A suitable model plant for control of the set fuel cell-DC/DC converter. *Renew. Energy* **2008**, *33*, 813–826. [CrossRef]
3. Barbir, F.; Molter, T.; Dalton, L. Efficiency and weight trade-off analysis of regenerative fuel cells as energy storage for aerospace applications. *Int. J. Hydrogen Energy* **2005**, *30*, 351–357. [CrossRef]
4. Wilberforce, T.; Alaswad, A.; Palumbo, A.; Dassisti, M.; Olabi, A.G. Advances in stationary and portable fuel cell applications. *Int. J. Hydrogen Energy* **2016**, *41*, 16509–16522. [CrossRef]
5. Fadzillah, D.M.; Kamarudin, S.K.; Zainoodin, M.A.; Masdar, M.S. Critical challenges in the system development of direct alcohol fuel cells as portable power supplies: An overview. *Int. J. Hydrogen Energy* **2019**, *172*, 207–219. [CrossRef]
6. Serincan, M.F. Validation of hybridization methodologies of fuel cell backup power systems in real-world telecom applications. *Int. J. Hydrogen Energy* **2016**, *42*, 19129–19140. [CrossRef]
7. Kuo, J.K.; Wang, C.F. An integrated simulation model for PEM fuel cell power systems with a buck DC-DC converter. *Int. J. Hydrogen Energy* **2011**, *36*, 11846–11855. [CrossRef]
8. Fabbri, E.; Bi, L.; Pergolesi, D.; Traversa, E. Towards the next generation of solid oxide fuel cells operating below 600 °C with chemically stable proton-conducting electrolytes. *Adv. Mater.* **2012**, *24*, 195–208. [CrossRef]
9. Slah, F.; Mansour, A.; Hajer, M.; Faouzi, B. Analysis, modeling and implementation of an interleaved boost DC-DC converter for fuel cell used in electric vehicle. *Int. J. Hydrogen Energy* **2017**, *42*, 28852–28864. [CrossRef]
10. Thounthong, P.; Raël, S.; Davat, B. Test bench of a PEM fuel cell with low voltage static converter. *J. Power Sources* **2006**, *153*, 145–150. [CrossRef]
11. Palma, L.; Todorovic, M.H.; Enjeti, P. A high gain transformerless DC-DC converter for fuel cell applications. In Proceedings of the Annual IEEE Conference on Power Electronics Specialists (PESC), Dresden, Germany, 16 June 2005; pp. 2514–2520.
12. Gerard, M.; Poirot-Crouzevier, J.P.; Hissel, D.; Pera, M. Ripple current effects on PEMFC aging test by experimental and modeling. *J. Fuel Cell Sci. Technol.* **2011**, *8*, 021004. [CrossRef]
13. Valdez-resendiz, J.E.; Sanchez, V.M.; Rosas-caro, J.C.; Mayomaldonado, J.C.; Sierra, J.M.; Barbosa, R. Continuous input-current buck-boost DC-DC converter for PEM fuel cell applications. *Int. J. Hydrogen Energy* **2017**, *42*, 30389–30399. [CrossRef]
14. Pathapati, P.R.; Xue, X.; Tang, J. A new dynamic model for predicting transient phenomena in a PEM fuel cell system. *Renew. Energy* **2005**, *30*, 1–22. [CrossRef]
15. Moreira, M.V.; da Silva, G.E. A practical model for evaluating the performance of proton exchange membrane fuel cells. *Renew. Energy* **2009**, *34*, 1734–1741. [CrossRef]
16. Al-Baghdadi, M.S. Modelling of proton exchange membrane fuel cell performance based on semiempirical equations. *Renew. Energy* **2005**, *30*, 1587–1599. [CrossRef]
17. Arasaratnam, I. A simplified design, control and power management of fuel cell vehicles. *SAE Tech. Pap.* **2014**. [CrossRef]
18. Han, J.; Charpentier, J.F.; Tang, T. An energy management system of a fuel cell/battery hybrid boat. *Energies* **2014**, *7*, 2799–2820. [CrossRef]
19. Motapon, S.N. A Generic Fuel Cell Model and Experimental Validation. Master's Thesis, École de Technologie Supérieure (ÉTS), Montreal, QC, Canada, 2008.
20. Bizon, N.; Mazare, A.G.; Ionescu, L.M.; Enescu, F.M. Optimization of the proton exchange membrane fuel cell hybrid power system for residential buildings. *Energy Convers. Manag.* **2018**, *163*, 22–37. [CrossRef]
21. Christou, A.G. Hydrogen Fuel Cell Power System Performance of Plug Power Gen Core 5B48 Unit. Master's Thesis, University of Strathclyde, Glasgow, Scotland, 2010.
22. O'Hayre, R.; Cha, S.W.; Colella, W.; Brinz, F.B. *Fuel Cell Fundamentals*; Wiley: New York, NY, USA, 2006.
23. Abd El Monem, A.A.; Azmy, A.M.; Mahmoud, S.A. Effect of process parameters on the dynamic behavior of polymer electrolyte membrane fuel cells for electric vehicle applications. *Ain Shams Eng. J.* **2014**, *5*, 75–84. [CrossRef]
24. Kunusch, C.; Puleston, P.; Mayosky, M. *Sliding-Mode Control of PEM Fuel Cells*; Springer: London, UK, 2012.
25. Jianfeng, H.; Liangfei, X.; Xinfan, L.; Languang, L.; Minggao, O. Modeling and experimental study of PEM fuel cell transient response for automotive applications. *Tsinghua Sci. Technol.* **2009**, *14*, 639–645.

26. Hwang, J.J.; Kuo, J.K.; Wu, W.; Chang, W.R.; Lin, C.H.; Wang, S.E. Life cycle performance assessment of fuel cell/battery electric vehicles. *Int. J. Hydrogen Energy* **2013**, *38*, 3433–3446. [CrossRef]

27. Motapon, S.N.; Tremblay, O.; Dessaint, L.A. Development of a generic fuel cell model: Application to a fuel cell vehicle simulation. *Int. J. Power Electron.* **2012**, *4*, 505–522. [CrossRef]

28. Bicer, Y.; Dincer, I.; Aydin, M. Maximizing performance of fuel cell using artificial neural network approach for smart grid applications. *Energy* **2016**, *116*, 1205–1217. [CrossRef]

29. Haibo, Q.; Yicheng, Z.; Yongtao, Y.; Li, W. Analysis of buck–boost converters for fuel cell electric vehicles. In Proceedings of the IEEE International Conference on Vehicular Electronics and Safety (ICVES), Shanghai, China, 13–15 December 2006; pp. 109–113.

30. Prudente, M.; Pfitscher, L.L.; Emmendoerfer, G.; Romaneli, E.F.; Gules, R. Voltage multiplier cells applied to non-isolated DC-DC converters. *IEEE Trans. Power Electron.* **2008**, *23*, 871–887. [CrossRef]

31. Hu, X.; Gong, C. A high voltage gain dc–dc converter integrating coupled-inductor and diode–capacitor techniques. *IEEE Trans. Power Electron.* **2014**, *29*, 789–800.

32. Schimpf, F.; Norum, L.E. Grid connected converters for photovoltaic, state of the art, ideas for improvement of transformerless inverters. In Proceedings of the Nordic Workshop on Power and Industrial Electronics (NORPIE), Espoo, Finland, 9–11 June 2008.

33. Palma, L.; Todorovic, M.H.; Enjeti, P. Design considerations for a fuel cell powered dc–dc converter for portable applications. In Proceedings of the Annual IEEE Conference on Applied Power Electronics Conference and Exposition (APEC), Dallas, TX, USA, 19–23 March 2006; pp. 19–23.

34. Ali, M.S.; Kamarudin, S.K.; Masdar, M.S.; Mohamed, A. An overview of power electronics applications in fuel cell systems: DC and AC converters. *Sci. World J.* **2014**, *2014*, 103709. [CrossRef]

35. Meng, H. Synchronous or Nonsynchronous Topology? Boost System Performance with the Right DC-DC Converter. Maxim Integrated® Application Note. Available online: http://www.maximintegrated.com/en/design/technical-documents/app-notes/6/6129.html (accessed on 14 May 2022).

36. Romadhon, M.I.; Andromeda, T.; Facta, M.; Warsito, A. A comparison of synchronous and nonsynchronous boost converter. *IOP Conf. Ser. Mater. Sci. Eng.* **2017**, *190*, 012021. [CrossRef]

37. Martinez, W.; Imaoka, J.; Itoh, Y.; Yamamoto, M.; Umetani, K. Analysis of coupled-inductor configuration for an interleaved high step-up converter. In Proceedings of the International Conference on Power Electronics (ICPE), Seoul, Korea, 1–5 June 2015; pp. 2591–2598.

38. Kosai, H.; McNeal, S.; Page, A.; Jordan, B.; Scofield, J.; Ray, B. Characterizing the effects of inductor coupling on the performance of an interleaved boost converter. In Proceedings of the Annual Passive Components Conference (CARTS), Jacksonville, FL, USA, 30 March 2009; pp. 237–251.

39. Rahavi, J.S.A.; Kanagapriya, T.; Seyezhai, R. Design and analysis of interleaved boost converter for renewable energy source. In Proceedings of the International Conference on Computing, Electronics and Electrical Technologies (ICCEET), Nagercoil, India, 21–22 March 2012; pp. 447–451.

40. Seyezhai, R.; Mathur, B.L. Design and implementation of interleaved boost converter for fuel cell systems. *Int. J. Hydrogen Energy* **2012**, *37*, 3897–3903. [CrossRef]

41. Kabalo, M.; Paire, D.; Blunier, B.; Bouquain, D.; Simoes, M.G.; Miraoui, A. Experimental evaluation of four-phase floating interleaved boost converter design and control for fuel cell applications. *IET Power Electron.* **2013**, *6*, 215–226. [CrossRef]

42. Kabalo, M.; Blunier, B.; Bouquain, D.; Miraoui, A. State-of-the-art of DC/DC converters for fuel cell vehicles. In Proceedings of the IEEE Conference on Vehicle Power and Propulsion (VPPC), Lille, France, 1–3 September 2010; pp. 1–6.

43. Garrigos, A.; Sobrino-Manzanares, F. Interleaved multi-phase and multi-switch boost converter for fuel cell applications. *Int. J. Hydrogen Energy* **2015**, *40*, 8419–8432. [CrossRef]

44. Xu, W.; Cheng, K.W.; Chan, K.W. Application of Cuk converter together with battery technologies on the low voltage DC supply for electric vehicles. In Proceedings of the International Conference on Power Electronics Systems and Applications (ICPESA), Hong Kong, China, 15–17 December 2015; pp. 1–5.

45. Huang, W.; Yen, K.; Roig, G.; Lee, E. Voltage divided noninverting Cuk converter with large conversion ratios. In Proceedings of the IEEE Southeastcon, Williamsburg, VA, USA, 7–10 April 1991; pp. 1005–1007.

46. Salah, W.; Taib, S.; Al-Mofleh, A. Development of multistage converter for outdoor thermal electric cooling (TEC) applications. *Jordan J. Mech. Ind. Eng.* **2010**, *4*, 15–20.

47. Alavi, O.; Viki, A.H.; Bina, M.T.; Akbari, M. Reliability assessment of a stand-alone wind-hydrogen energy conversion system based on thermal analysis. *Int. J. Hydrogen Energy* **2017**, *42*, 14968–14979. [CrossRef]

48. Ciappa, M.; Carbognani, F. Lifetime prediction and design of reliability tests for high power devices in automotive applications. *IEEE Trans. Device Mater. Reliab.* **2003**, *3*, 191–196. [CrossRef]

49. Ma, K.; Liserre, M.; Blaabjerg, F.; Kerekes, T. Thermal loading and lifetime estimation for power device considering mission profiles in wind power converter. *IEEE Trans. Power Electron.* **2015**, *30*, 590–602. [CrossRef]

50. Strickland, P.R. The thermal equivalent circuit of a transistor. *IBM J. Res. Dev.* **1959**, *3*, 35–45. [CrossRef]

51. Alavi, O.; Abdollah, M.; Viki, A.H. Assessment of thermal network models for estimating IGBT junction temperature of a buck converter. In Proceedings of the Power Electronic and Drive Systems and Technologies Conference (PEDSTC), Mashhad, Iran, 14–16 February 2017; pp. 102–107.

52. Hnatek, E.R. *Practical Reliability of Electronic Equipment and Products*; CRC Press: New York, NY, USA, 2002.

53. Wintrich, A.; Nicolai, U.; Tursky, W.; Reimann, T. *Application Manual Power Semiconductors*; Semikron International GmbH: Nuremberg, Germany, 2011.
54. Chung, H.S.H.; Wang, H.; Blaabjerg, F.; Pecht, M. *Reliability of Power Electronic Converter Systems*; Institution of Engineering and Technology: London, UK, 2015.
55. Cui, H. Accelerated temperature cycle test and Coffin–Manson model for electronic packaging. In Proceedings of the Annual Symposium on Reliability and Maintainability (RAMS), Alexandria, VA, USA, 24–27 January 2005; pp. 556–560.
56. Busca, C.; Teodorescu, R.; Blaabjerg, F.; Munk-Nielsen, S.; Helle, L.; Abeyasekera, T.; Rodriguez, P. An overview of the reliability prediction related aspects of high power IGBTs in wind power applications. *Microelectron. Reliab.* **2011**, *51*, 1903–1907. [CrossRef]
57. Wang, B.; Cai, J.; Du, X.; Zhou, L. Review of power semiconductor device reliability for power converters. *CPSS Trans. Power Electron. Appl.* **2017**, *2*, 101–117. [CrossRef]
58. Sadigh, A.K.; Dargahi, V.; Abarzadeh, M.; Dargahi, S. Reduced DC voltage source flying capacitor multicell multilevel inverter: Analysis and implementation. *IET Power Electron.* **2014**, *7*, 439–450. [CrossRef]
59. Hwang, C.L.; Yoon, K.P. *Multiple Attribute Decision Making: Methods and Applications*; Springer: New York, NY, USA, 1981.
60. Behzadian, M.; Khanmohammadi Otaghsara, S.; Yazdani, M.; Ignatius, J. A state-of the-art survey of TOPSIS applications. *Expert Syst. Appl.* **2012**, *39*, 13051–13069. [CrossRef]
61. Opricovic, S.; Tzeng, G.H. Compromise solution by MCDM methods: A comparative analysis of VIKOR and TOPSIS. *Eur. J. Oper. Res.* **2004**, *156*, 445–455. [CrossRef]